Influence of texture and test velocity on the dynamic, high-strain, tensile behavior of zirconium

J.P. Escobedo *, E.K. Cerreta, C.P. Trujillo, D.T. Martinez, R.A. Lebensohn, V.A. Webster, G.T. Gray III

MST-8, Los Alamos National Laboratory, Los Alamos, NM 87545, USA

Abstract

Experiments were conducted to characterize the influence of texture and impact velocity on the dynamic, high-strain, tensile extrusion of zirconium. Bullet-shaped samples were machined from a clock-rolled, highly textured Zr plate. Specimens in two orthogonal directions were tested: the extrusion direction aligned with either the in-plane (IP) rolling or the through-thickness (TT) direction of the plate. The post-extrusion microstructure and texture evolution were examined using electron backscatter diffraction microscopy and modeled using the viscoplastic self-consistent model. It was found that extrusion deformation was accomplished through a combination of twinning and slip with their relative activity greatly depending on the initial texture. In this regard, higher elongations in the IP samples as compared to the TT samples were observed at similar test velocities. This difference in ductility is discussed in terms of the material's ability to accommodate plastic deformation. Due to the availability of a larger number of slip systems with relatively high Schmid factors in the IP samples under this configuration, plastic deformation by prismatic slip can be easily achieved, resulting in larger elongations. On the contrary, for TT samples, twinning preceded deformation by slip. This sequential deformation process, driven by the need to reorient the microstructure favorably to slip, led to diminished elongations to failure.

1. Introduction

Zirconium (Zr) has received considerable attention in numerous investigations due to its relatively high ductility, good corrosion resistance and low absorption of neutrons. These properties, in particular, make Zr attractive to the nuclear and chemical industries [1,2]. To understand the deformation response and observed texture evolution during various types of mechanical loadings, the substructural evolution of Zr has been studied in numerous investigations, primarily under uniaxial stress conditions [3–9]. The mechanical response of high-purity Zr has been shown to be sensitive to interstitial content, grain size, texture, temperature and strain rate. Increasing strain rates and decreasing temperatures have been shown to lead to increased yield stresses and work-hardening rates [10]. Additionally, for high-purity, clock-rolled plates [10] the uniaxial stress response has been shown to display a higher yield stress in the through-thickness (TT) direction of the plate as compared to specimens loaded along a direction within the plane of the plate, referred to as an in-plane (IP) specimen. Additionally, the effect of the rolling texture yields an initially parabolic work-hardening behavior that transitions to a "concave-up" behavior when loaded in IP compression and a "concave-down" work-hardening when loaded in TT compression [11]. This is reversed in the tensile case.

The influences of strain rate, temperature and texture on the mechanical response have all been explained in terms of

---

* Corresponding author. Tel.: +1 509 592 0180.
  E-mail address: jpescobedo@lanl.gov (J.P. Escobedo).

the relative activation of twinning vs. slip [6]. In this regard, Zr single crystals, like other ductile, hexagonal close-packed (hcp) metals does not possess in general the five soft independent slip systems, therefore deformation is accommodated through a combination of slip and twinning [12]. For Zr, the most commonly observed slip systems are the prismatic ($\{1\,0\,\bar{1}\,0\}\langle 1\,\bar{2}\,1\,0\rangle$) and to a lesser extent the pyramidal ($\{1\,\bar{1}\,0\,1\}\langle 1\,1\,\bar{2}\,0\rangle$ and $\{1\,1\,\bar{2}\,2\}\langle 1\,1\,\bar{2}\,\bar{3}\rangle$) systems. Notably, basal slip is not typically observed in high-purity Zr. The most frequently observed twin systems are the $\{1\,\bar{1}\,0\,2\}\langle 1\,0\,\bar{1}\,\bar{1}\rangle$ and $\{1\,1\,\bar{2}\,1\}\langle 1\,1\,\bar{2}\,\bar{6}\rangle$ tensile twins, and the $\{1\,1\,\bar{2}\,2\}\langle 1\,1\,\bar{2}\,\bar{3}\rangle$ compressive twins. The designation "tensile twin" indicates that for a given c/a ratio, the twin accommodates $\langle c\rangle$-axis expansion in the hcp crystallographic unit cell; the opposite is the case for "compressive" twins [3,4]. The relative activation of these systems has been an active area of study with appreciable contributions by Tomé and co-workers [1,13–16]. It has been shown that under most loading conditions, prismatic slip is dominant and activation of both prismatic and pyramidal slip systems is highly dependent upon loading direction with respect to the texture of the material. Additionally, pyramidal slip may be important in regions of high stress concentrations. Just as for slip, twin activation is highly dependent upon loading direction for a highly textured Zr specimen but is also highly sensitive to stress state as deformation twinning is dependent upon the sense of shear. This has been shown by Bingert et al. [17] where the Schmid factors have been plotted as a function of the angle between applied load and the basal pole for Zr loaded in tension and compression.

The effects of shock prestrain on the mechanical response of Zr have been investigated by Cerreta et al. [18], who observed that shock prestraining Zr to a peak shock stress below the alpha to omega high-pressure phase transition ($\sim$7.1 GPa) obeys the Cottrel–Stokes law [19] and thus exhibits no enhanced hardening. However, for specimens shock prestrained to peak shock stresses above the alpha to omega phase transition, an enhanced hardening behavior was observed as compared to as-annealed Zr. This was attributed to reduced available glide distances within the microstructure due to significant twinning, retained metastable omega phase and stored dislocations within the substructure.

Although considerable work has been devoted to examining the mechanical response of Zr deformed in uniaxial stress states, and to a lesser extent some work has been dedicated to understanding the response of Zr under uniaxial strain, relatively little is understood about the behavior of Zr under more complex loading conditions. Additionally, while considerable attention has been paid to the compressive behavior of highly textured Zr as a function of loading direction, there is a lack of tensile data particularly in the high-strain and high-strain-rate regimes. Therefore, the purpose of this study has been to investigate the dynamic tensile extrusion response of Zr subjected to large plastic strains. The influence of texture and impact velocity on

the microstructure and texture evolution has been characterized in detail in order to understand the response of Zr under this complex loading condition.

2. Experimental methods

2.1. Material characterization

The metallurgical characterization of the initial and post-extrusion microstructures of the Zr samples was performed using optical microscopy and electron backscatter diffraction (EBSD) microscopy. In preparation for these measurements, each piece was mounted in an epoxy resin and the surface was prepared by standard metallographic procedures to a 4000 grit SiC finish followed by chemical polishing with a solution comprising $45H_2O$:$45HNO_3$: 10HF. The samples were then polished with a mixture of 10 parts of 0.05 μm colloidal silica and 1 part of H_2O_2 to minimize the relief caused by the chemical attack. EBSD microscopy was performed on a Phillips XL30 FEG equipped with TSL data acquisition software. The instrument was operated at 20 kV and a spot size of 5. For the local texture determination, orientation measurements were performed with a step size of 2 μm over two or three large areas (250 μm × 500 μm), and the results were then averaged. The purpose of this procedure was to mimic bulk texture measurements, such as those performed by neutron diffraction. Orientation measurements using a smaller step size of 0.2 μm were performed to characterize the fine details of the microstructure and their evolution before and after the extrusion deformation; measurements were performed two or three times on a given area to test reproducibility and generate a statistically valid representation of the deformation fields.

All targets were prepared from clock-rolled and annealed, high-purity Zr. Clock-rolling is a multiple pass rolling sequence in which the plate is rotated to various multiples of 45° between passes (Fig. 1a). The plate was then annealed at 550 °C for 1 h in vacuum to produce a fully recrystallized and homogeneous microstructure. The initial characterization of the Zr plate is shown in Fig. 1; the orientation (Fig. 1b) and texture (Fig. 1c) results are presented with respect to the through-thickness (TT) direction of the plate. A microstructure with an average grain size of 15–20 μm is measured. The plate exhibits a strong basal texture aligned with the TT direction (Fig. 1c). Approximately 90% of the orientation measurements of the angle between the $\langle c\rangle$-axis and the TT direction show a deviation of less than 40°, as shown in the distribution graphs in Fig. 1d. The chemical composition of the Zr studied is given in Table 1.

2.2. Dynamic extrusion experiments

Dynamic tensile extrusion tests were conducted in a modified 7.62 mm diameter Taylor cylinder apparatus [20]. The schematic of the experimental configuration is
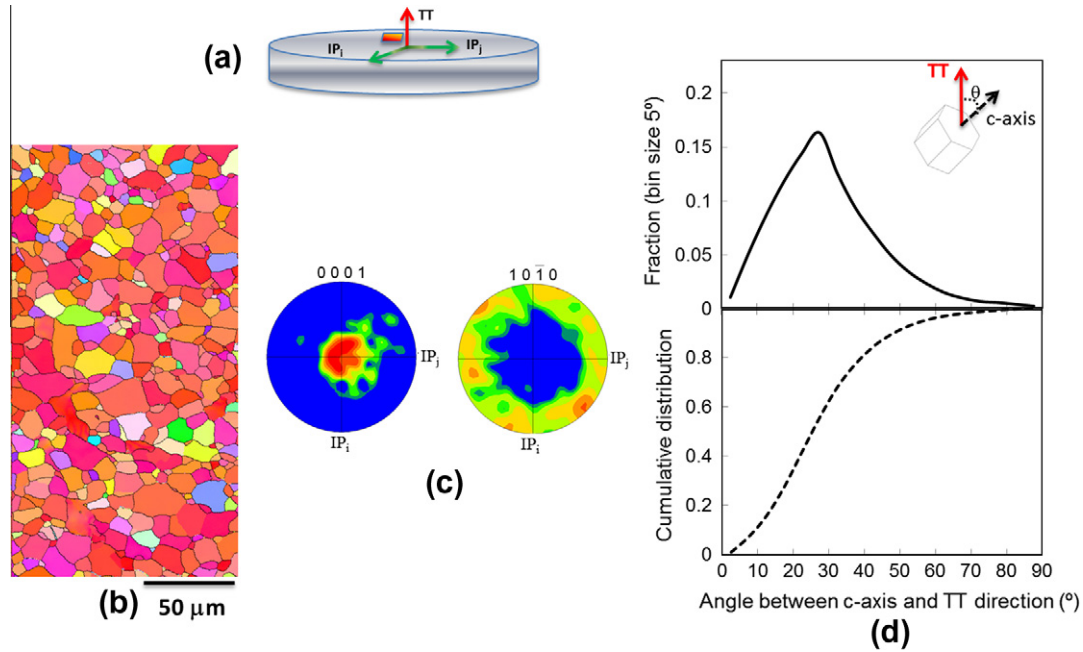
Fig. 1. (a) Schematic of the clocked-rolled Zr plate. (b) Orientation map of the microstructure with the sample normal aligned with the {TT} direction. (c) Pole figure showing texture of annealed material. (d) Distribution of ⟨c⟩-axis orientation with respect to the {TT} direction.

Table 1
Chemistry of the zirconium plate (wt. ppm).

Element							
Al	C	Fe	Hf	N	O	Ti	V
20	30	263	37	10	50	25	25

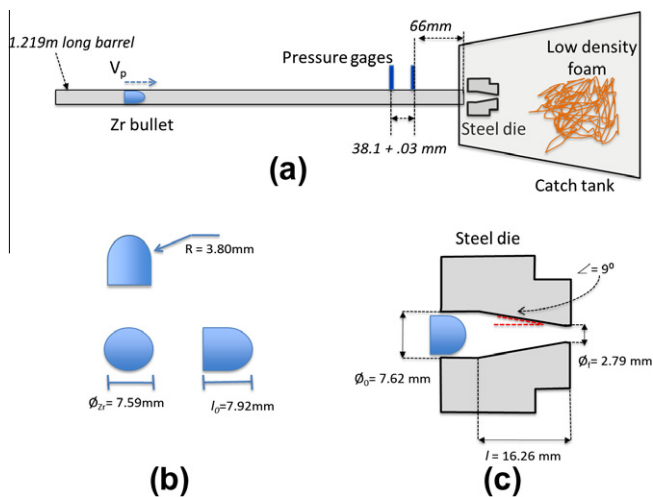All values are equal to or less than the values given above.

Fig. 2. (a) Schematic of experimental configuration. (b) Geometry of the Zr bullets. (c) Schematic of the steel die.

shown in Fig. 2a. The barrel is 1219 mm long with two machined holes that hold piezoelectronic pressure transducers. The holes are 38.1 mm apart from each other with a machine tolerance of 0.03 mm. The distance between the second transducer and the extrusion die is 66 mm. The

pressure readings were recorded on a Tektronik TDS744 digitizer with a sample rate of 2 GS s^{-1}. The specifications of the pressure transducers used are less than 1 μs rise time. Thus, the error in the measurements is not greater than 1.5% or 6–9 m s^{-1} for the velocity range of the experiments pursued in this study (400–600 m s^{-1}). Preliminary photon Doppler velocimetry (PDV) data, focused on the axis of the barrel, determined that the sample was already at terminal velocity when it crossed the area where the pressure transducers are mounted. The velocity measured using PDV correlated well with velocity measured using pressure transducers [21]. Bullet-shaped specimens were fired and the fully extruded pieces were soft recovered by decelerating them in a low-density foam. The in situ extrusion process was captured using high-speed photography [20–22]. All recovered pieces from each shot were weighed and compared to the starting bullet weight to ensure that no segments were lost during recovery.

The dimensions of the bullets are shown in Fig. 2b. Two types of specimens were machined: (1) with the long axis of the bullet parallel to the normal of the plate or TT direction; and (2) with the long axis of the bullet perpendicular to the normal of the plate or IP direction. Bullets were accelerated in a He-gas launcher at speeds in the 400–600 m s^{-1} range, and impacted into a high-strength steel extrusion die (A2 or S7 tool steel with a Rockwell Hardness of 56 and 54, respectively). Dies were designed with an entrance diameter of 7.62 mm and an exit diameter of 2.79 mm (Fig. 2c). Upon impact, the die geometry imposed an oblique shockwave in the Zr samples. For the upper limit velocity of 600 m s^{-1} and considering the mass impedances (density and sound speeds) of the steel die and Zr

samples, a shock match of ~3.5 GPa for the shock peak stress, along with associated shear stresses, is calculated for these specimens. Calculations were based on techniques reported by Cao et al. [22]. This stress is well below the value of ~7.1 GPa necessary to induce the α–ω phase transition observed in shock-loaded high-purity Zr [18].

3. Results

3.1. High-speed photography and total elongation

Representative high-speed photography results of experiments at two velocities are shown in Fig. 3a and b. Images similar to these were utilized to reassemble extruded segments from all tests conducted in this study. In all cases, specimens were not fully extruded and a piece remained in the die after the test was complete. The piece remaining in the die (hereafter referred to as "Piece 1") and all fully extruded pieces are shown in the correct sequence in the micrographs in Fig. 3c and d. When examining the high-speed photography and stereographic images, it is observed that with increasing impact velocity, the propensity for plastic instability increased. This resulted in more segments or sample particulation during the extrusion.

From the reassembled segments, total elongations were calculated. The total elongation as a function of the impact velocity for the two tested textures is shown in Fig. 4. To establish statistically reliable trends, from the total number of experiments (~22 for each direction), six groups were created with each group containing the elongation measurements of two or three experiments for which impact velocity was within 7 m s^{-1}, a value close to the uncertainty in the velocity measurement. For the two tested directions, an increase in total elongation with increasing impact velocity is observed in Fig. 4. Additionally, for any given impact velocity, the IP specimens display relatively higher total elongations than the TT samples. To further support these observations, an analysis of variance (two-way
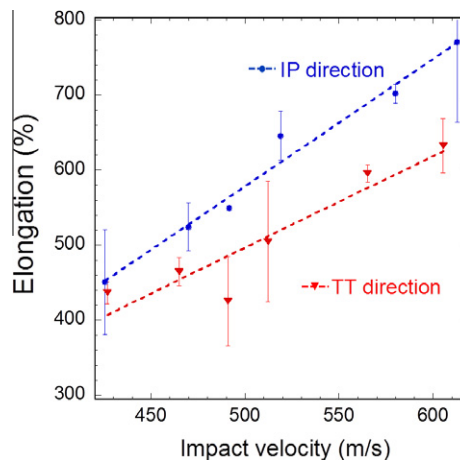

Fig. 4. Elongation (%) vs. impact velocity.

ANOVA) of the experimental data was performed considering the impact velocity and texture factors. The analysis yielded P-values of <0.0001 for the velocity, <0.0005 for the texture. With a P-value <0.05 necessary to establish any statistical trend or difference, these results quantitatively support the trend observed in Fig. 4: both velocity and the texture have significant effects in the total elongation experienced by the samples during dynamic extrusion, and they are mutually independent.

The higher elongations in the IP samples with respect to the TT samples, at similar test velocities, may be rationalized in terms of the dominant deformation modes under the current loading configuration. Due to the texture possessed by the specimens, extrusion deformation was achieved primarily by an applied tensile load orthogonal to the basal poles for the IP case, whereas the load direction was aligned parallel to the average orientation of the basal poles in the TT case. Under these conditions, as shown in Bingert et al. [17], higher Schmid factors are calculated for the prismatic slip systems in the IP samples as
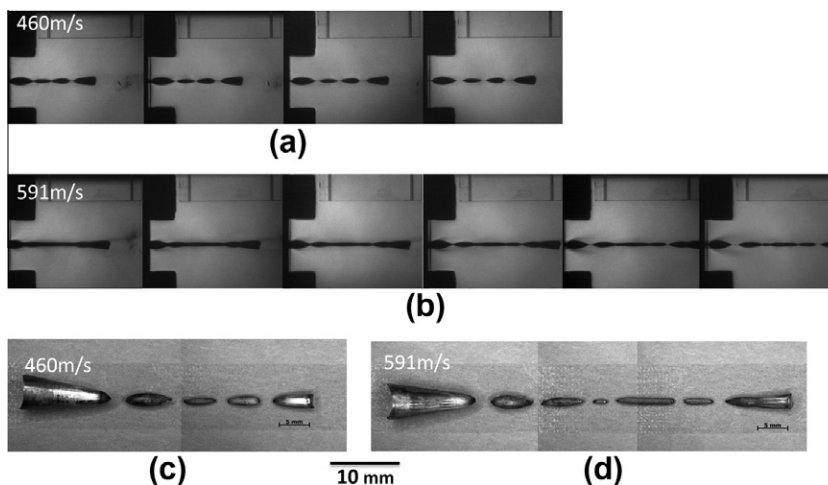

Fig. 3. (a and b) High speed photography showing the sequence in which samples exited the die after extrusion. (c and d) Stereographic images of reassembled Zr specimens.

compared to the TT samples. This availability of high Schmid factor slip systems is likely to lead to more slip activation, and, hence, larger elongations are expected for the IP cases. In the following sections we present experimental evidence, as well as modeling, that supports this scenario.

3.2. SEM and optical microscopy

For all experiments, a significant amount of recrystallization was observed to dominate the microstructure in all pieces that exited the die. These results suggest that these pieces exhibit an advanced deformation stage and adiabatic heating during the extrusion process. Hence, a thorough examination of Piece 1 was pursued in this study to elucidate the mechanisms during the early and subsequent stages of extrusion deformation. In this regard, due to the lateral constraints imposed by the steel die, in all tests Piece 1 was forced to adopt a final shape similar to the die (conical with an opening angle of ∼18°). This condition was observed throughout the piece, except at the back free surface and the tip of this piece. As both of these regions correspond to free surfaces of the specimen, these regions were allowed to exhibit any inherent material response dictated by the initial, highly textured microstructure. In what follows, the results of the characterization efforts to probe these two regions are presented.

Scanning electron microscopy (SEM) images of the fracture surfaces of Piece 1 are shown in Fig. 5. In the TT cases, an isotropic (round in shape) fracture surface is observed (Fig. 5a and b). In contrast, the fracture surface of the IP case (Fig. 5c and d) is oval in shape, and the superimposed arrows show the orientation of the original basal poles. Similar ovalization has been observed in highly textured Zr IP samples deformed under quasi-static tension. This effect is qualitatively explained in terms of the relatively easier prismatic slip [11,15,16] for this specimen orientation under this stress state.

To further elucidate the effect of initial texture on the overall deformation process, samples from the TT and IP orientations were prepared to expose two perpendicular cross-sections for each case. Each of these orthogonal planes contained the extrusion direction. Optical micrographs corresponding to Piece 1 of two TT samples (Fig. 6a) extruded at similar velocities are shown in Fig. 6b and c. A similar overall contour, specifically the wavy contour of the back free surface of the segment, is observed in both samples, independent of the plane exposed. Conversely, for the IP samples (Fig. 6e), depending on the plane exposed, two different contours are observed, as shown in Fig. 6f and g. While a contour similar to that observed in the TT cases is observed in Fig. 6f, a perpendicular section shows a different profile, with a back free surface with a concave contour (Fig. 6g). These observations are shown schematically in Fig. 6d and h and will be further discussed later in this section in the context of EBSD measurements.
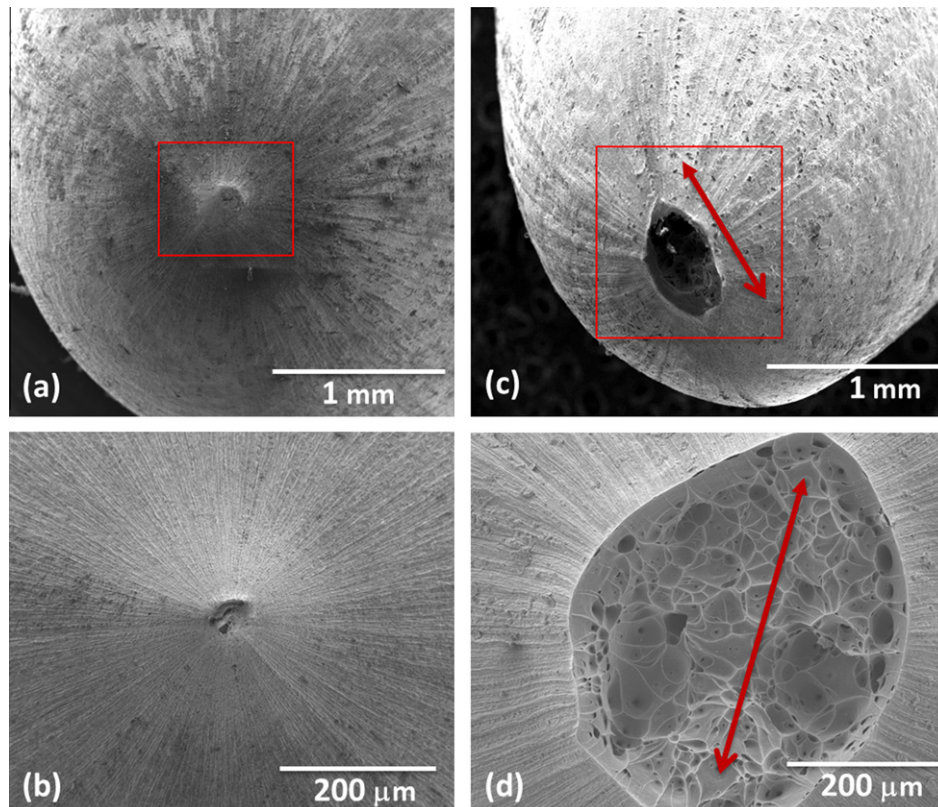

Fig. 5. SEM images of the fracture surfaces of Piece 1. (a and b) TT case. (c and d) IP case.
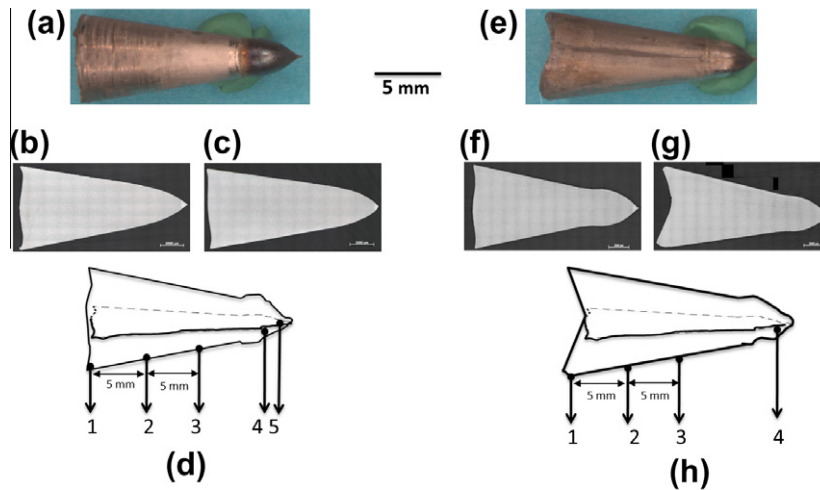
Fig. 6. Macroscopic shape details in deformed specimens. (a–d) TT case. (e–h) IP case.

By using optical micrographs, width measurements were taken every ~5 mm from the back free surface of Piece 1 for locations 1–3 (hereafter referred to as Regions 1–3) and then at two select places close to the tip: Regions 4 and 5. This is shown schematically in Fig. 6d and h. Due to the shape of the bullets, the strain calculation for a given region was performed by estimating how much volume was stuck in the die from the back free surface to the location of the region. Then, by considering conservation of volume it was possible to track back the dimensions of the original diameter of the cross-section of a given region. Based on these considerations, the true strains were calculated to be 0.25–0.35 for Region 1, 0.55–0.65 for Region 2, 0.95–1.05 for Region 3, and about 3.5 and 5 for Regions 4 and 5, respectively. These calculated strains can be used as relative indicators of the local extent of deformation. Details of the microstructure as a function of deformation in these areas are discussed next.

3.3. EBSD characterization

3.3.1. Microstructure as a function of deformation

A series of optical micrographs and representative EBSD orientation maps of the cross-section of Piece 1 for specimens tested at impact velocities of ~600 m s^{-1} in the IP and TT directions are shown in Figs. 7 and 8, respectively. As indicated by the texture keys in Figs. 7 and 8, the orientation and texture maps are presented such that the TT direction corresponds to the sample normal direction, represented as the center of the direct pole figures in the texture plots. The extrusion direction is projected onto the transverse direction (TD) for the IP maps and onto the center of the pole figures in the TT cases. In addition, the EBSD measurements were taken in the interior, close to the centerline of the sample, away from the shaded regions shown in the optical micrographs (Figs. 7a and 8a). The shaded regions mark the areas affected by frictional forces between the Zr samples and the die. By utiliz-

ing optical micrographs, the width of these regions affected by friction was measured to be no more than 100 μm for all cases.

For the IP case, an equiaxed grain structure is seen to be preserved in Region 1 of Piece 1 (Fig. 7b). A continuous evolution of the grain structure from equiaxed to progressively elongated, to recrystallized grains is observed along the extrusion direction (Fig. 7b–e). This gradient in microstructure in Piece 1 was representative of all the tested TT and IP specimens, independent of shot velocity. It should be noted in the IP case, the deformed microstructures preserved the (0 0 0 1) texture similar to the annealed Zr plate. However, for the TT case, a clear difference is observed in the crystallographic orientation of the microstructures in all regions. The texture has significantly shifted from the original basal (0 0 0 1) shown in Fig. 1b and c to a strong (1 0 $\bar{1}$ 0) pole parallel to the extrusion direction (Fig. 8g–j). Further details for each region are discussed next.

While some similarities in microstructural evolution were observed amongst all specimens, metallographic analyses revealed significant differences in deformation mechanisms activated in each specimen. In Region 1, which experienced local strains of 0.25–0.35, the main differences between the IP and TT cases are the presence of twins easily identified in the IP case (Fig. 7b) and by the shift in texture for the TT case (Fig. 8g). These observations can be explained in terms of the volume fraction of twinned material in each case. Quantified measurements of twinning are presented in the next section.

After the clear texture shift that occurs in Region 1 of the TT case, Regions 2 and 3 of both the IP and TT cases display similar microstructures. In Region 2, which experienced strains in the 0.55–0.65 range, the microstructures exhibit elongated grains aligned parallel to the extrusion direction (Figs. 7c and 8c). The textures show a strong (1 0 $\bar{1}$ 0) component along the extrusion direction (Figs. 7g and 8h). In Region 3, with larger calculated strains of ~1, grains with larger elongation are observed (Figs. 7d
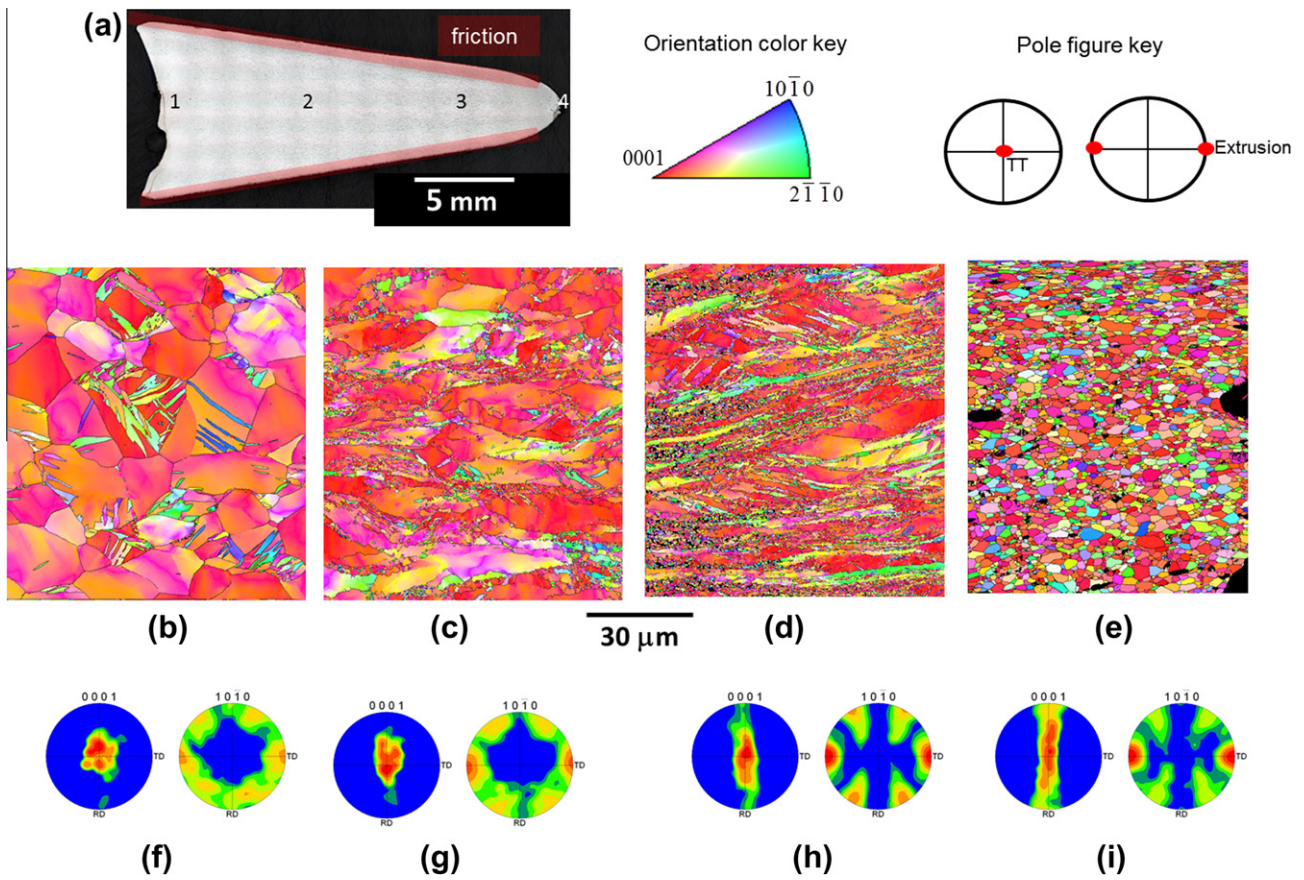
Fig. 7. IP specimen. (a) Optical image of Piece 1. Orientation maps of Regions (b) 1, (c) 2, (d) 3 and (e) 4. (f–i) Corresponding pole figures of Regions 1–4 showing the development of $(1\,0\,\bar{1}\,0)$ fiber texture during extrusion along TD.

and 8d). The textures in these regions possess a somewhat stronger $(1\,0\,\bar{1}\,0)$ fiber developing along the extrusion direction (Figs. 7h and 8i).

Region 4 for both IP (Fig. 7e) and TT specimens (Fig. 8e) show deformation-free microstructures with average grain sizes of ~4 μm. The deformation-free microstructures, lacking intragranular misorientation, likely result from the competition between grain annealing, associated with thermal processes due to adiabatic heating, and grain refinement due to the large strain (>3) mechanical deformation [23,24]. It should be noted that for the majority of the IP cases, Region 4 corresponds to the tip of Piece 1.

For the TT specimen, there is an additional Region 5 (Fig. 8f) at the tip of Piece 1. The microstructure in this region shows larger grains with no clear preferred orientation (Fig. 8k). It should be noted that the IP samples experienced the higher strains. It could be possible that a similar microstructure might have also been developed at the tip of these samples, but then lost during the more catastrophic rupture process due to the larger strains experienced by the IP samples as compared to the TT samples for a given shot velocity. The details of a likely mechanism to explain the microstructure in this region are discussed later in this paper.

3.3.2. Microstructure as a function of impact velocity

Additional EBSD-based analyses were performed on Region 1 of the IP and TT specimens to investigate the effect of impact velocity on microstructural evolution; specific focus was on the propensity of twinning as a function of test velocity (i.e. strain rate [16]). However, due to the extensive plastic deformation experienced by the extruded samples, with strains in the 0.25–0.35 range for Region 1, the characterization of individual twinning modes was not possible by conventional approaches such as that reported in McCabe et al. [25], as those methods require proper identification of a parent grain–daughter twin pair. However, based on the premise that any tensile twinning process reorients the $\langle c \rangle$-axis by at least 64.2° [4,25,26], the EBSD data can be partitioned to selectively analyze the orientation measurements with crystallographic orientations of ~75° or greater away from the original $(0\,0\,0\,1)$ pole orientation. The threshold value for the angle value was taken to be larger than the minimum 64° to compensate for spread in the original distribution of the $\langle c \rangle$-axes (Fig. 1d). Using this scheme, the twinned fractions can be indirectly extracted.

The orientation maps for Region 1 of IP specimens tested at ~428 and ~592 m s^{-1} are shown in Fig. 9a and
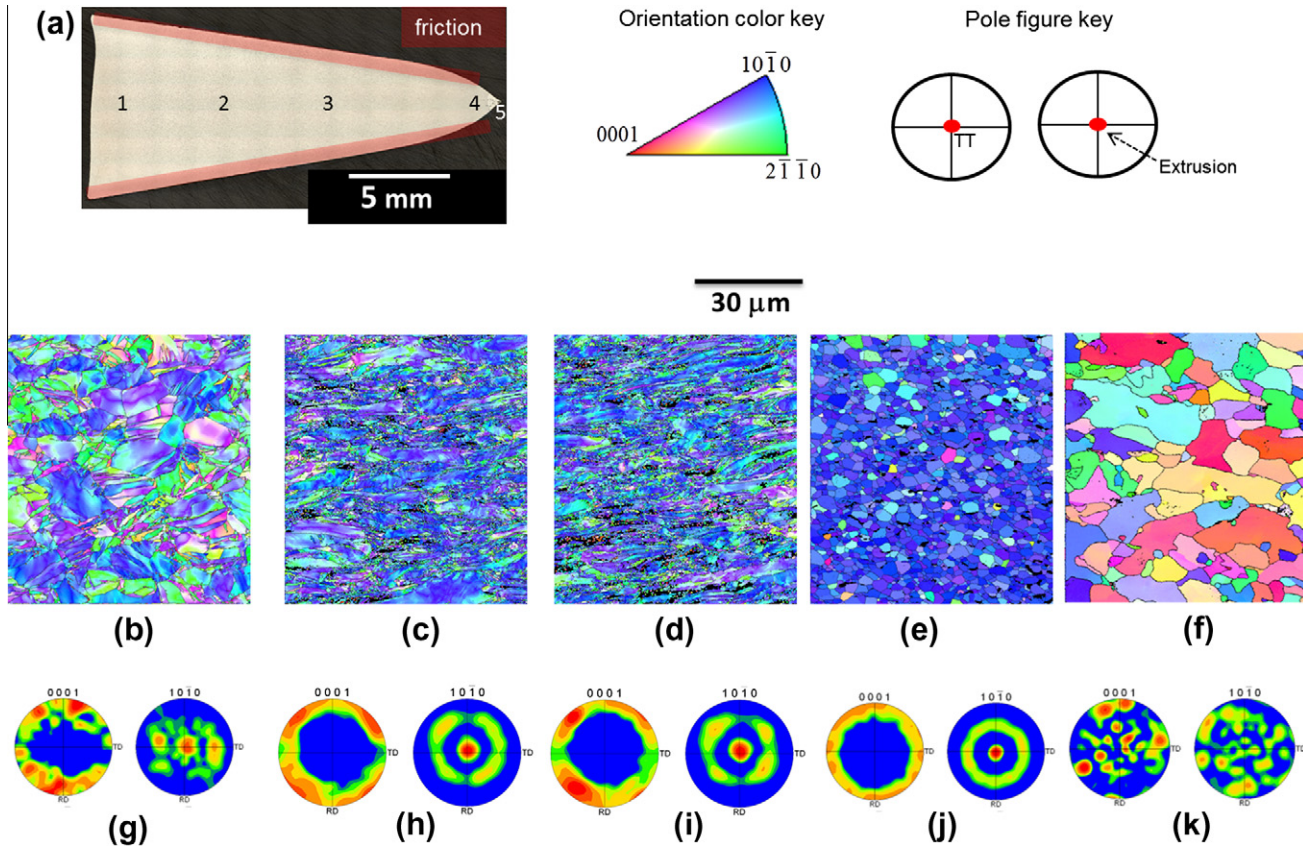
Fig. 8. TT specimen. (a) Optical image of Piece 1. Orientation maps of Regions (b) 1, (c) 2, (d) 3, (e) 4 and (f) 5 (g–j) Corresponding pole figures of Regions 1–4 showing the development of $(1\,0\,\bar{1}\,0)$ fiber texture during extrusion. (k) Pole figure of Region 5 showing a randomized texture.

b, respectively. By using the scheme just detailed, the twinned fractions were measured to be ∼3% for the sample deformed at 422 m s^{-1} (Fig. 9c), increasing to ∼6% as the velocity increased to 592 m s^{-1} (Fig. 9d). For both cases, the amount of twinning was not significant enough to cause an extensive reorientation of the (0 0 0 1) poles, and therefore the textures in this region remained relatively unchanged with respect to the original texture, as shown in Fig. 9e. The orientation distribution plot in Fig. 9f shows a more quantified measurement. Slight differences are observed in the distribution of the ⟨c⟩-axes with respect to the annealed structure. For instance, there is a small increase in the right tail of the distribution as signaled by the arrow. This increase in the fraction of orientations away from the (0 0 0 1) pole has been associated with compressive twinning for this specific specimen orientation [25].

The results from similar, selective measurements performed in TT samples tested at 422 and 600 m s^{--1} are shown in Fig. 10a and c. A value of ∼0.78 for the twinned fraction was measured for both cases. This significant shift in the texture from the original basal (0 0 0 1) to a strong $(1\,0\,\bar{1}\,0)$ parallel to the extrusion direction, as observed in Fig. 10e, has been qualitatively explained by the activation of $\{1\,\bar{1}\,0\,2\}$ tensile twins that reorient the crystals by 85.22° [17,25–27]. The velocity does not seem to significantly affect the amount of twinning for the TT case. Thus, to further assess the effect of test velocity, grain misorientation maps,

generally associated with plastic deformation, are presented in Fig. 10c and d. A larger degree of plastic deformation is observed in the sample deformed at 600 m s^{-1} (Fig. 10d) as compared with the one deformed at 422 m s^{-1} (Fig. 10b). These measurements correlate with the more well-defined $(1\,0\,\bar{1}\,0)$ texture developed at 600 m s^{-1} as shown in Fig. 10e. The quantification of these measurements in the orientation distribution plot (Fig. 10f), further confirms these observations. For both velocities, substantial reorientation of the ⟨c⟩-axes by 85° is observed in Fig. 10f, and then the fraction of reoriented ⟨c⟩-axes is observed to increase with increasing impact velocity, further strengthening the $(1\,0\,\bar{1}\,0)$ texture.

These findings, i.e. (i) a lack of difference in twin volume fraction as a function of velocity but (ii) a significant difference as a function of texture, suggest that, overall, the influence of impact velocity on microstructural evolution during dynamic extrusion was not as significant as the influence of texture. This is further evidenced by the development of macroscopic specimen morphologies previously shown in Fig. 6. These morphologies clearly reflect the texture evolution in each case. For instance, for the TT case it was observed that the deformed samples possess a microstructure with $(1\,0\,\bar{1}\,0)$ directions preferentially oriented along the extrusion direction and (0 0 0 1) directions oriented radially (Fig. 8h–k). Thus, as shown in Fig. 6d, any two given orthogonal planes are aligned with their
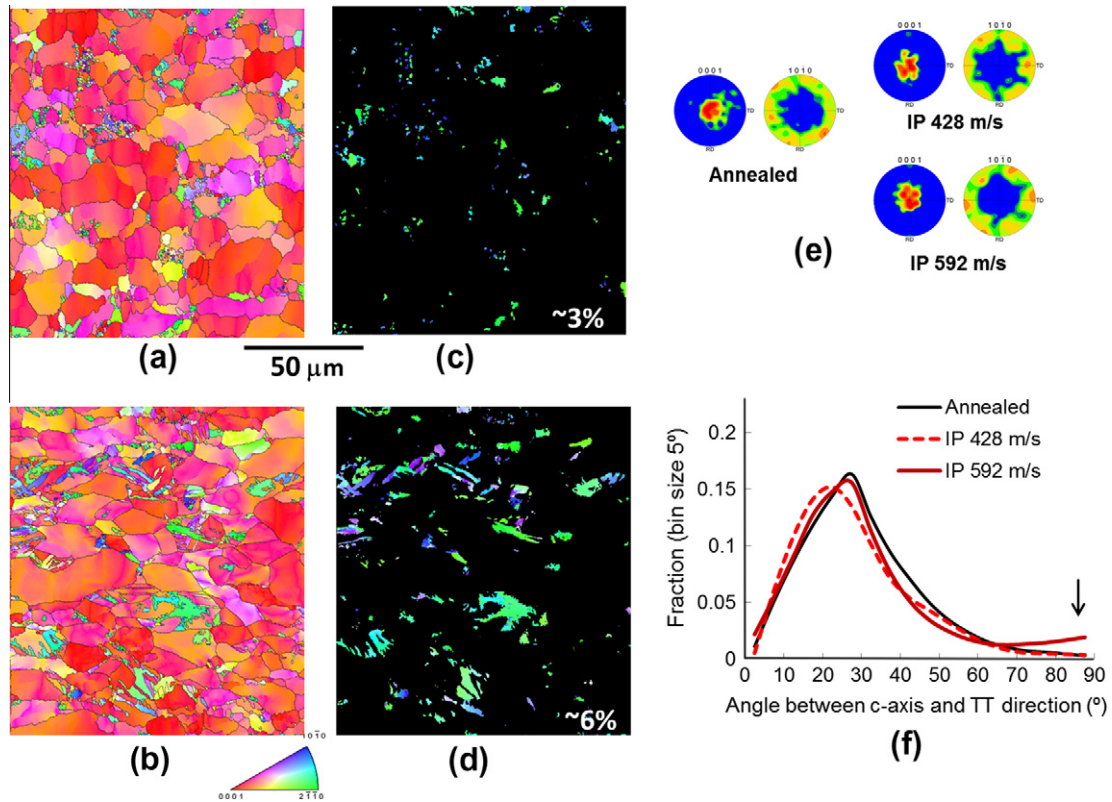
Fig. 9. Orientation maps of Region 1 in IP samples tested at (a) 428 m s^{-1}, (b) 592 m s^{-1}. (c and d) Corresponding maps showing only measurements with orientations greater than 75° away from the *c*-axis. (e) Texture plots from (a and b). (f) Distribution of the angle between *c*-axis and the TT direction.

normal parallel to the basal direction. Hence, the same contour can be observed at any given exposed plane. For the IP cases, it was found that the deformed samples retained a microstructure with a preferred (0 0 0 1) orientation along the original TT direction, while a (1 0 $\bar{1}$ 0) texture developed along the extrusion direction (Fig. 7f–i). This anisotropic behavior renders similar contours as the TT cases to any section parallel to the basal (0 0 0 1) direction (Fig. 6h) and a different contour for sections orthogonal to it.

3.3.3. Deformation modes

As shown in the previous section, information obtained in Region 1 provides an insight into the early stages of anisotropic deformation for this complex loading path and can aid in the identification of the predominant deformation mechanisms, i.e. twinning or slip, during the onset of the extrusion process. Unfortunately, as already stated, due to the large deformation, the assessment of individual deformation modes was not possible by any of the automated approaches using EBSD data reported in the literature [25,26]. However, as already introduced in Fig. 10c and d, the local variation in misorientation within individual grains is generally seen as an indicator of plastic strain in crystalline materials. Thus, by measuring misorientation within different grains, it was possible to infer the activity of individual deformation modes and, in

particular for this study, the activation of deformation modes with ⟨*c*⟩-component, such as pyramidal slip or twinning. Such modes are the signature of the reorientation of crystallites toward or away from the basal direction [25,27,28]. Misorientation vector profiles were measured on orientation maps from Region 1 and projected onto inverse pole figures. Three colors served to mark the activity of a deformation mode with ⟨*c*⟩-component within a grain. Blue lines correspond to tangential lines in the inverse pole figure and therefore are indicative of absence of ⟨*c*⟩-component. Red lines indicate the presence of a component towards the (0 0 0 1) pole. The gray color is used to indicate misorientation measured within twins.

The orientation map of Region 1 of an IP sample is shown in detail in Fig. 11a. Several misorientation profiles were measured along the directions indicated by the arrows and are shown as projected lines in the inverse pole figure in Fig. 11b. As depicted in Fig. 11b, most of the misorientation vector profiles are blue in color. This indicates that the activity of deformation modes with ⟨*c*⟩-components is either absent or kept at a minimal value. This observation further confirms that, for IP samples, prismatic slip dominated the deformation during the initial stages of extrusion.

The results for the TT case are shown in Fig. 12. The misorientation profiles in this case (Fig. 12b) show a significant activity of deformation modes with ⟨*c*⟩-component in the misorientation profile vectors measured within grains
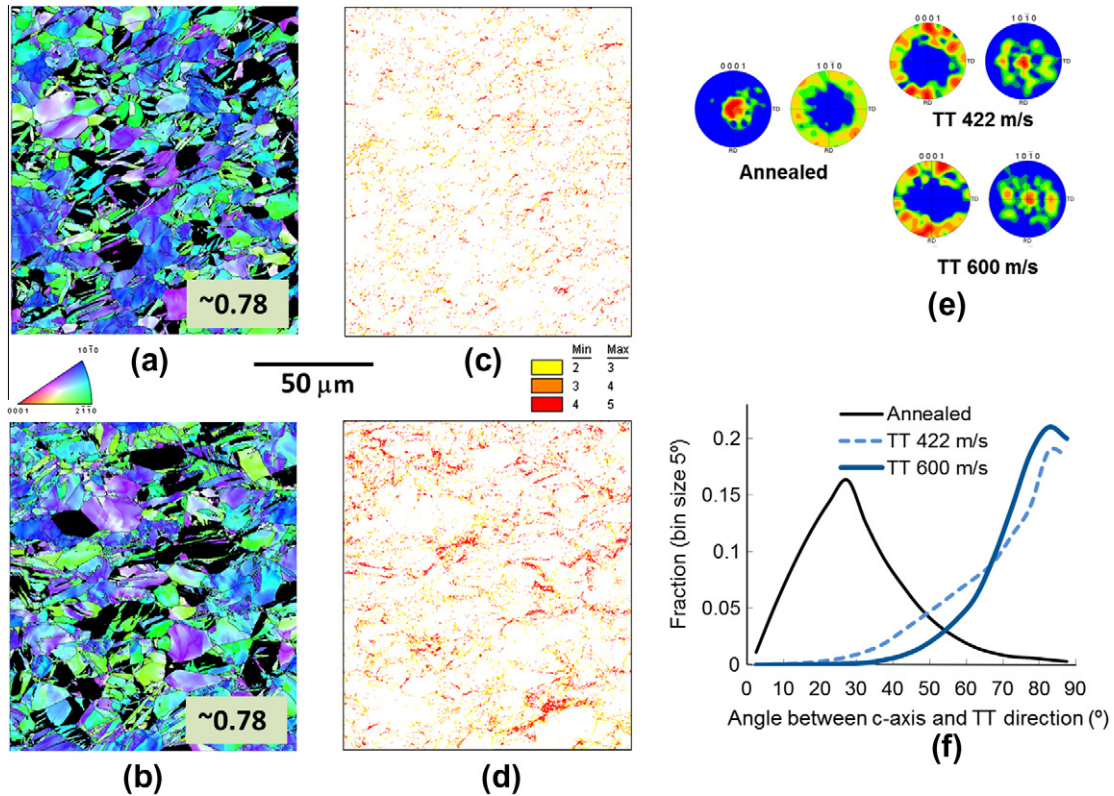
Fig. 10. Orientation maps of Region 1 in TT specimens showing only measurements with orientations greater than 75° away from the *c*-axis of samples tested at (a) 422 m s^{-1}, (b) 600 m s^{-1}. (c and d) Corresponding grain misorientation maps. (e) Texture plots from Region 1. (f) Distribution of the angle between *c*-axes and TT direction.
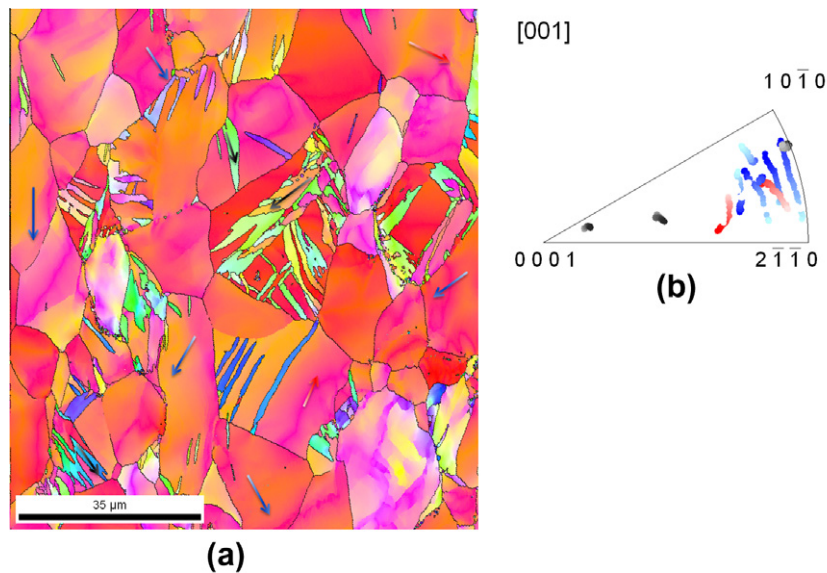

Fig. 11. (a) Orientation map and (b) inverse pole figures showing misorientation profiles of an IP specimen tested at 592 m s^{-1}. The color of the arrows in the orientation map is associated with the color of the lines in the IPF maps. (For interpretation of the references to colour in this figure legend, the reader is referred to the web version of this article.)

(red) and twins (gray). These results confirm that pyramidal slip and twinning are significantly active in these regions, causing a reorientation of the microstructure away from the ⟨*c*⟩-axis pole.

3.4. Modeling of texture evolution using VPSC

To further elucidate the contribution of each deformation mode responsible for the texture evolution, simula-
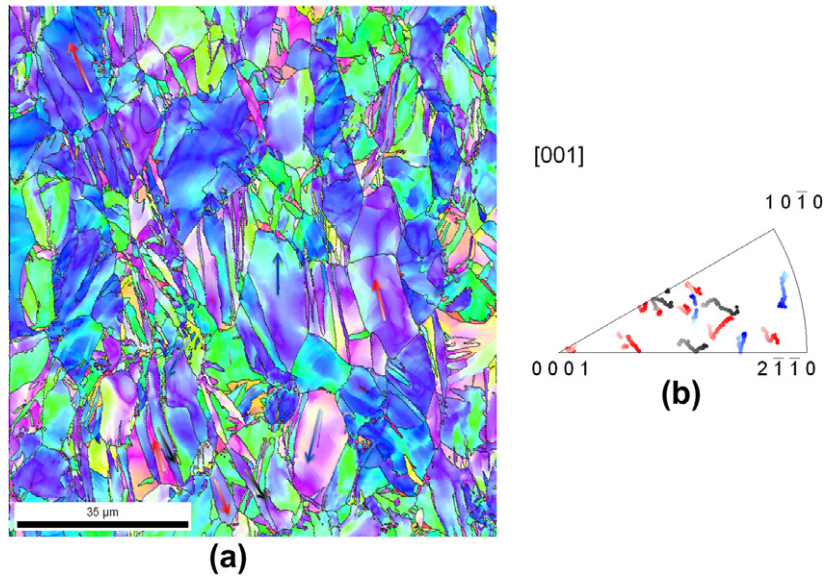
Fig. 12. (a) Orientation map and (b) inverse pole figures showing misorientation profiles of a TT specimen tested at 600 m s^{-1}. The color of the arrows in the orientation map is associated with the color of the lines in the IPF maps. (For interpretation of the references to colour in this figure legend, the reader is referred to the web version of this article.)

Table 2
Voce hardening parameters used for VPSC simulations.

Deformation mode	Voce hardening parameters			
	τ_0	τ_1	θ_0	θ_1
Prismatic slip	1	0.8	67.8	4.3
Pyramidal slip	7.6	10.2	88.6	39.5
Tensile twinning	5.4	0.9	5.3	1.6
Compressive twinning	14.2	1.6	52.6	44.7

tions of texture evolution based on polycrystal plasticity were performed using the viscoplastic self-consistent (VPSC) model developed by Lebensohn and Tomé [13]. Due to the lack of an adequate model to simulate recrystallization textures, only deformation textures, corresponding to Regions 1–3 were modeled.

The methodology consisted in utilizing the initial orientation map from Fig. 1b to generate a set of weighted orientations (based on grain size) as input textures for the model. The deformation modes used for the simulations were prismatic and pyramidal slip, and tensile and compressive twinning. Despite the obvious differences in strain rates between the present experiments and the quasistatic experiments of Tomé et al. [15,16], the same relative values of the initial critical resolved shear stresses of these modes

Table 3
Relative velocity gradient components used for VPSC simulations.

Sample	Velocity gradient components	
	$\dot{u}_{x,x}/\dot{u}_{z,z}$	$\dot{u}_{y,y}/\dot{u}_{z,z}$
TT	−0.5	−0.5
IP	−0.8	−0.2

were assumed, while the corresponding hardening parameters were slightly modified to better match the present observations on twinning activity and texture evolution. The adopted parameters, relative to the initial value of the prismatic critical resolved shear stress, are shown in Table 2. The type of boundary conditions applied to simulate the IP and TT cases are shown in Table 3. In the TT case, the velocity gradient tensor applied was such that the sample was extended in the normal direction, while volume conservation was achieved by imposing equal shortening of both transverse directions. For the IP case, the boundary conditions were based on the observation made on the ovalization of the fracture surfaces and the anisotropic shape of the cross-sections, indicating that larger strain occurs in the direction orthogonal to the ⟨c⟩-axis. It was found that the velocity gradient that best reproduces the experimental observations is one having a 1:4 ratio between the two transverse components, the smaller being along the ⟨c⟩-axis ($\dot{u}_{y,y}$ in Table 3, IP case).

The simulated textures for the IP case are shown in Fig. 13a–c; the strains are as indicated. The simulated textures correlate well with the measured textures corresponding to Regions 1–3 (Fig. 13d–f). The relative activity of the different deformation modes is shown in Fig. 13g. The calculated activity for each mode is consistent with the experimental observations that deformation is dominated primarily by prismatic (prism) slip, with limited contribution of twinning (tensile and compressive) and pyramidal slip (pyr). This type of deformation causes the basal pole to remain invariant while the (1 0 $\bar{1}$ 0) poles are aligned parallel with the extrusion axis (TD), as measured experimentally (Fig. 13d–f) and in simulation (Fig. 13a–c). In addition, the calculated twinned fraction at a 0.30 strain
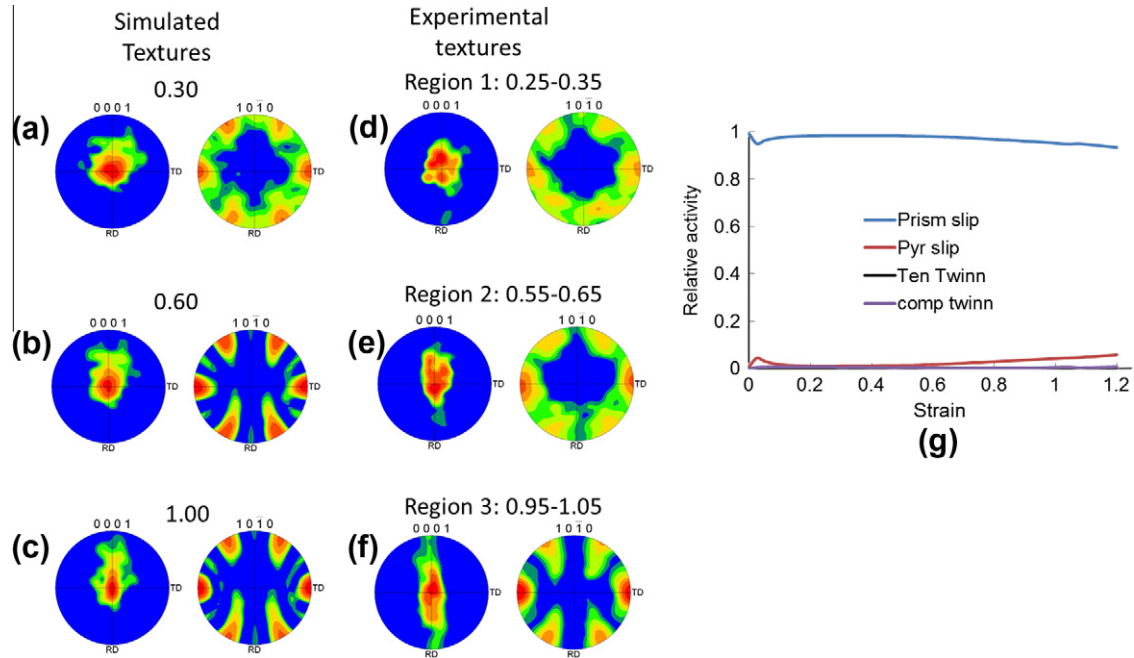
Fig. 13. Pole figures for the IP case at the indicated regions and strains. (a–c) Simulated. (d–f) Experimental. (g) Relative activity of individual deformation modes calculated using VPSC.
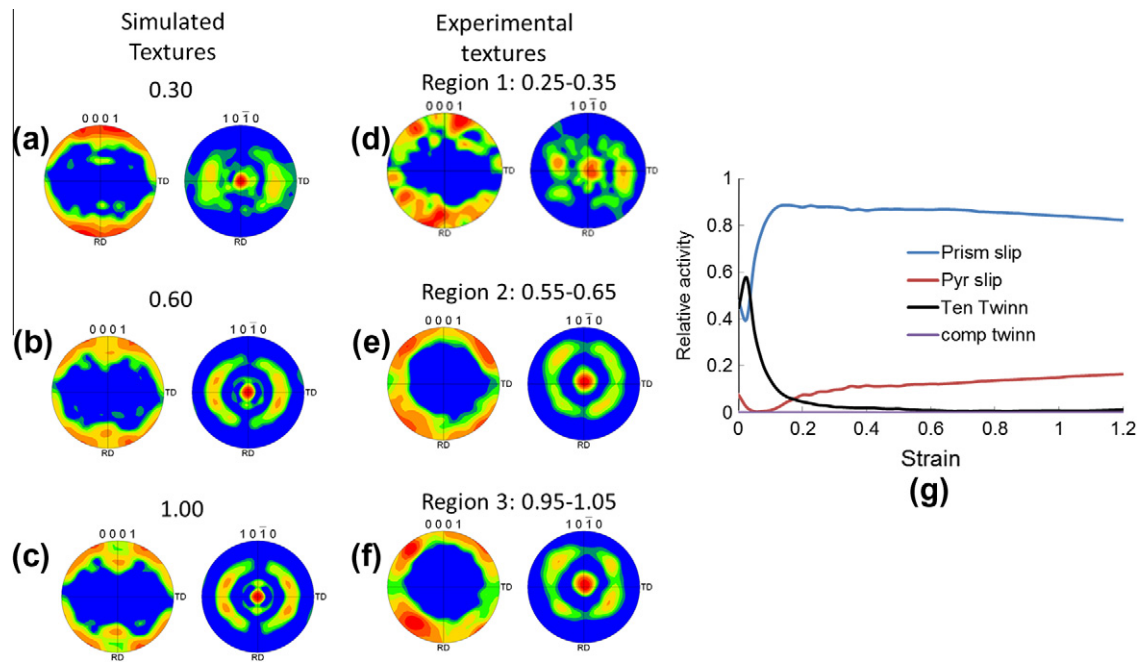

Fig. 14. Pole figures for the TT case at the indicated regions and strains. (a–c) Simulated. (d–f) Experimental. (g) Relative activity of individual deformation modes calculated using VPSC.

is 2.8%, close to the experimentally measured value of 3% for the sample deformed at 422 m s⁻¹.

The results of the extrusion simulations for the TT case are given in Fig. 14a–c, the strains are as indicated. Good agreement between the simulated and the measured textures from Regions 1–3 (Fig. 14d–f) is observed. The (0 0 0 1) poles are predominantly orthogonal to the extrusion axis (pole center), while a strong (1 0 ī 0) component

clearly develops parallel to the extrusion axis (pole center). The relative activity of the different deformation modes (slip and twinning) is shown in Fig. 14g. These results confirm the experimental observations that at the early stages of extrusion deformation, tensile twinning is very active (with a peak at ∼0.05 strain). Then, as strain increases beyond ∼0.05, there is a gradual decrease in twinning activity, while both prismatic and pyramidal slip start to domi-

nate the deformation. For this case, the calculated twinned fraction at 0.3 strain is 82%, close to the 78% measured experimentally. Compressive twinning remains close to inactive throughout the simulations.

4. Discussion

The dynamically extruded IP specimens displayed consistently higher total elongations compared with the TT samples at a given velocity; however, instability and sample fragmentation as a function of shot velocity did not significantly differ for the two orientations. The experimental observations and the calculated activity of deformation modes, using VPSC, show clearly that in both the IP and TT cases, extrusion deformation is accommodated via a combination of slip and twinning. However, the degree of twinning is significantly higher in the TT compared to the IP specimens. In the IP cases, due to the availability of slip systems with high Schmid factor with respect to the extrusion direction, the samples accommodate deformation through prismatic slip and scattered twinning during tensile loading [11]. Interestingly, this results in greater total elongations for a given shot velocity in IP specimens as compared to TT specimens.

Conversely, the samples extruded along the TT direction, first develop a microstructure by lattice reorientation prior to prismatic slip. This reorientation is attained primarily due to extensive tensile twinning and contributions from pyramidal slip. Once the crystallites are reoriented, further deformation is dominated by prismatic slip, strengthening the development of the $(1\,0\,\bar{1}\,0)$ texture fiber. These results establish the chronological sequence in the deformation processes during extrusion deformation.

The process of grain elongation (Regions 2 and 3) leading to grain refinement and recrystallization (Region 4) was not only observed in Piece 1, but also throughout all the fully extruded segments. This type of severe grain deformation leading to grain refinement and recrystallization has also been observed under other complex loading conditions, such as mechanical testing of hat-shaped specimens [23,29]. Other studies have suggested that this process takes place through a mechanical, subgrain rotation process aided by a deformation-induced adiabatic heating [23,24].

Significant grain coarsening and texture randomization were observed at the tip of Piece 1 in all the TT cases, and sporadically in smaller areas in a few IP specimens. A viable mechanism to explain the emergence of new orientations is as follows: adiabatic heating, induced by plastic work, causes a temperature increase that likely causes the material to undergo a α to β phase transformation [30,31]. This inference is supported by the fact that this necked region has sustained true strains larger than 5.0. This would create regions not only experiencing the largest increases in temperature but also the largest strains and strain rates in the entire bullet. It follows that the largest concomitant plastic deformation causes the highest dislocation activity. The latter should be responsible for the creation of high-angle grain boundaries but also crystal reorientation [32]. This combined effect of deformation and temperature increase causes a loss of texture memory, normally seen when Zr samples undergo α–β–α phase transformations in exclusive heat-treatment experiments [30]. After rupture, the stress state drops to zero in this region and the sample is allowed to undergo static annealing, i.e. recovery and grain growth. This sequential process could potentially render the coarse, randomly oriented microstructures observed in this study.

5. Conclusions

Based upon the present study of the influence of texture and test velocity on the dynamic-tensile extrusion of high-purity Zr, the following conclusions can be drawn:

- Extrusion deformation was accomplished through a combination of twinning and slip. Their relative activities are seen to depend on the initial texture. In this regard, TT samples showed a higher propensity for tensile twinning, primarily during the early stages of deformation (Region 1).
- The subsequent larger deformation (Regions 2 and 3) was achieved primarily by prismatic slip as measured experimentally and modeled by VPSC. It should be noted that development of texture was irrespective of the initial texture. All specimens tested in this current study developed a $(1\,0\,\bar{1}\,0)$ extrusion texture.
- The total elongation increased with increasing test velocity. Higher elongations in the IP samples were observed with respect to the TT samples, at similar test velocities. The difference in tensile ductility between the two orientations may be rationalized in terms of the dominant deformation modes. A relatively larger number of available slip systems with higher Schmid factor exists for the IP samples as compared with the TT samples. The enhanced availability of high Schmid factor slip systems led to more slip activation, and, hence, larger elongations were measured in the IP specimens.

Currently, experiments are being performed at high temperatures to investigate the effect of temperature in promoting plastic deformation by dislocation slip. In addition, in situ diagnostics are continuing to be developed to measure the real-time response, during extrusion deformation, complementing high-speed photography. In particular, the use of PDV systems is being employed to capture the motion of the front end of the bullet [21,33]. Significant results of these measurements and their implication for microstructure evolution will be reported in due course.

Acknowledgments

References

[1] Bhattacharyya D, Cerreta EK, McCabe RJ, Niewczas M, Gray GT, Misra A, et al. Acta Mater 2009;57:305–15.

[2] Schemel JH. ASTM manual on zirconium and hafnium. West Conshohocken, PA: ASTM International; 1977.

[3] Yoo MH. Met Mater Trans A – Phys Met Mater Sci 1981;12A:409–15. 1981.

[4] Partridge PG. Metall Rev 1967;12:169–94.

[5] Mason TA, Bingert JF, Kaschner GC, Wright SI, Larsen RJ. Met Mater Trans A – Phys Met Mater Sci 2002;33:949–54.

[6] Song SG, Gray GT. Met Mater Trans A – Phys Met Mater Sci 1995;26(10):2665–75.

[7] Rapperport EJ, Hartley CS. Trans Metall Soc AIME 1960;218:869–77. 1960.

[8] Chen SR, Gray GT. J. Phys IV France 1997;7(Colloque C3). C3-741–6.

[9] Baldwin DH, Reed-Hill RE. Trans Metall Soc AIME 1965;233:248–9.

[10] Kaschner GC, Gray GT. Met Mater Trans A – Phys Met Mater Sci 2000;31(8):1997–2003.

[11] Addessio LB, Cerreta E, Gray GT. Met Mater Trans A – Phys Met Mater Sci 2005;36A:2893–903.

[12] Kocks UF, Westlake DG. Trans Metall Soc AIME 1967;239:1107–9.

[13] Lebensohn RA, Tome CN. Acta Met Mater 1993;41(9):2611–24.

[14] Lebensohn RA, Tome CN. Philos Mag A 1993;67(1):187–206.

[15] Tomé CN, Maudlin PJ, Lebensohn RA, Kaschner GC. Acta Mater 2001;49(15):3085–96.

[16] Kaschner GC, Bingert JF, Liu C, Lovato ML, Maudlin PJ, Stout MG, et al. Acta Mater 2001;49(15):3097–108.

[17] Bingert JF, Mason TA, Kaschner GC, Maudlin PJ, Gray GT. Metall Mater Trans A 2002;33(3):955–63.

[18] Cerreta E, Gray GT, Hixson R, Rigg PA, Brown DW. Acta Mater 2005;53:1751–8.

[19] Homeycomb RWK. The plastic deformation of metals. London: Edward Arnold; 1968.

[20] Gray GT, Cerreta EK, Yablinsky CA, Addessio LB, Henrie BL, Sencer BH, et al. In: Presented at the shock compression of condensed matter; 2005 (unpublished).

[21] Trujillo CP, Martinez DT, Burkett MW, Escobedo JP, Cerreta EK, Gray III GT. AIP Conf Proc 2012;1426:406.

[22] Cao F, Cerreta EK, Trujillo CP, Gray GT. Acta Mater 2008;56(19):5804–17.

[23] Dougherty L, Cerreta E, Pfeif E, Trujillo C, Gray III G. Acta Mater 2007;55:6356–464.

[24] Liss KD, Garbe U, Li HJ, Schambron T, Almer JD, Yan K. Adv Eng Mater 2009;11(8):637–40.

[25] McCabe RJ, Proust G, Cerreta EK, Misra A. Int J Plast 2009;25(3):454–72.

[26] McCabe RJ, Cerreta EK, Misra A, Kaschner GC, Tome CN. Philos Mag 2006;86(23):3595–611.

[27] Tenckhoff E. In: Zirconium in the nuclear industry: 14th international symposium, vol. 1467; 2005. p. 25–50.

[28] Tenckhoff E. Z Metallkd 1972;63(4):192.

[29] Xue Q, Beyerlein IJ, Alexander DJ, Gray GT. Acta Mater 2007;55(2):655–68.

[30] Wenk HR, Lonardelli I, Williams D. Acta Mater 2004;52(7):1899–907.

[31] Crepin J, Bretheau T, Caldemaison D. Acta Met Mater 1995;43(10):3709–19.

[32] Chauvy C, Barberis P, Montheillet F. Recrystall Grain Growth 2004;467–470(Pts 1 and 2):1151–6.

[33] Trujillo CP, Escobedo-Diaz JP, Gray GT, Cerreta EK, Martinez DT. Dynamic behavior of materials, vol. 1. New York: Springer Verlag; 2011. p. 467–9.